Adsorption and Deactivation Characteristics of Cu/ZnO-Based Catalysts for Methanol Synthesis from Carbon Dioxide

Sittichai Natesakhawat[a,b,*] **· Paul R. Ohodnicki, Jr.**[a] **· Bret H. Howard**[a] **· Jonathan W. Lekse**[a] **· John P. Baltrus**[a] **· Christopher Matranga**[a]

[a]National Energy Technology Laboratory, United States Department of Energy, P.O. Box 10940, Pittsburgh, Pennsylvania 15236, USA

[b]Department of Chemical and Petroleum Engineering, University of Pittsburgh, Pittsburgh, Pennsylvania 15261, USA

*Corresponding author, e-mail: Sittichai.Natesakhawat@NETL.DOE.GOV

Abstract

The adsorption and deactivation characteristics of coprecipitated Cu/ZnO-based catalysts were examined and correlated to their performance in methanol synthesis from CO_2 hydrogenation. The addition of Ga_2O_3 and Y_2O_3 promoters is shown to increase the Cu surface area and CO_2/H_2 adsorption capacities of the catalysts and enhance methanol synthesis activity. Infrared studies showed that CO_2 adsorbs spontaneously on these catalysts at room temperature as both mono- and bi-dentate carbonate species. These weakly bound species desorb completely from the catalyst surface by 200 °C while other carbonate species persist up to 500 °C. Characterization using N_2O decomposition, X-ray diffraction (XRD), X-ray photoelectron spectroscopy (XPS), and transmission electron microscopy (TEM) with energy-dispersive X-ray spectroscopy (EDX) analysis clearly indicated that Cu sintering is the main cause of catalyst deactivation. Ga and Y

promotion improves the catalyst stability by suppressing the agglomeration of Cu and ZnO particles under pretreatment and reaction conditions.

Keywords Methanol · Carbon dioxide · Hydrogenation · Copper · Zinc oxide · Synergy · Sintering

1 Introduction

Due to ever-increasing concerns over energy demands and global warming, current research activities are driven by a pressing need to develop new, efficient technologies for mitigating CO_2 emissions. Thermocatalytic hydrogenation of CO_2 offers an attractive route to utilize CO_2 as an inexpensive raw material to produce value-added methanol, which can be used directly as a fuel or further converted to various commodities. While many catalytic systems including supported precious metal catalysts have been investigated, Cu/ZnO-based catalysts remain the most promising system for methanol synthesis from CO_2 [1,2]. There is a long-standing debate in the literature regarding the nature/identity of active sites, support/promoter effects, and reaction mechanisms [3]. Under typical operating conditions, the activity loss of these catalysts is attributed to thermal degradation via sintering of Cu particles [4-6]. ZnO is an important component because it prevents agglomeration of Cu particles, thus leading to the large Cu surface area needed for methanol catalysis. However, information about the crystal structure and morphology of ZnO, the synergy between Cu and ZnO, and how these properties affect the stability of such catalysts is lacking. Additionally, the role of ZnO on the adsorption and activation of CO_2 is still unclear [7,8]. Therefore, an understanding of adsorption and deactivation characteristics of Cu/ZnO-based catalysts will help identify key parameters

controlling their overall performance, both in activity and resistance to sintering, and will subsequently facilitate rational design of robust methanol synthesis catalysts for CO_2 reuse.

Previously, we have demonstrated that CO_2 hydrogenation to methanol over Cu-based catalysts is a structure-sensitive reaction [9]. There is a linear correlation between turnover frequency for methanol formation and Cu crystallite size. An activity enhancement observed with smaller Cu particles may be attributed to larger numbers of open planes and edge/defect sites that can bind more strongly with key reaction intermediates (i.e., formates). Moreover, we have verified that metallic Cu is the predominant Cu species on the surface of working catalysts, thereby excluding the possibility of Cu^+ species acting as active sites.

In the present contribution, we report a study of adsorption and deactivation characteristics of coprecipitated Cu/ZnO-based catalysts for methanol synthesis from CO_2. We investigated the nature of adsorbed species on the surface of reduced catalysts upon exposure to CO_2 and H_2 using temperature-programmed desorption (TPD) and diffuse reflectance infrared Fourier transform spectroscopy (DRIFTS). The sintering behavior of prepared catalysts was also examined by X-ray diffraction (XRD), X-ray photoelectron spectroscopy (XPS), high resolution transmission and scanning transmission electron microscopy (HRTEM/STEM), Cu surface area and dispersion measurements using N_2O decomposition, and temperature-programmed reaction (TPReaction). A promotional effect of Ga_2O_3 and Y_2O_3 addition on the CO_2/H_2 adsorption capacities and catalyst stability is discussed.

2 Experimental

2.1 Catalyst Preparation

Catalysts were prepared by a reverse coprecipitation method described in detail elsewhere [9]. The Cu/metal molar ratios were controlled during synthesis as follows: Cu/Zn ≈ 0.7 for the binary catalyst whereas Cu/Zn (Zr) ≈ 1.3 and Cu/Ga (Y) ≈ 2.7 for the ternary and multicomponent catalysts. CuO, ZnO, ZnO doped with Ga_2O_3 or Y_2O_3 (Zn/Ga (Y) = 2), and other pure metal oxide components were also synthesized in the same manner. All metal precursors (Aldrich) used were in a nitrate form. $NaHCO_3$ (0.1 M) was used for precipitating aqueous metal nitrate solutions and adjusting the pH of the precipitation medium to 7. After aging, washing, and drying steps, samples were calcined at 350 °C under air for 4 h. Table 1 lists actual metal contents in mol% of calcined catalysts determined by Inductively Coupled Plasma-Optical Emission Spectroscopy (ICP-OES).

2.2 Catalyst Characterization

BET surface areas of calcined catalysts were measured by N_2 adsorption at 77 K using a Quantachrome Autosorb 1-C. Prior to measurements, samples were degassed under vacuum at 110 °C overnight. BET surface areas of reduced catalysts were also determined after exposure to 10% H_2/Ar at 250 °C for 2 h using a Micromeritics Autochem 2950 HP.

Copper surface area and dispersion were measured by a nitrous oxide decomposition method using the Micromeritics Autochem 2950 HP. Copper dispersion is defined as the ratio of the surface copper atoms to the total copper atoms present in the catalyst. Initially, the catalysts (100 mg) were reduced in situ with 10% H_2/Ar at 250 °C for 2 h. The catalysts were then cooled to 60 °C and exposed to 10% N_2O/He for 1 h to oxidize surface copper atoms to Cu_2O. After

cooling to room temperature, temperature-programmed reduction (TPR) was performed under a 10% H_2/Ar flow to reduce Cu_2O back to metallic Cu using a ramp rate of 10 °C/min to 300 °C. Copper surface area and dispersion were calculated from the amount of H_2 consumed during the TPR step by assuming that copper crystallites are spherical and the Cu surface density equals 1.47×10^{19} atoms/m^2 [9]. Copper dispersion was also measured after consecutive reduction at 25 °C increments from 200 to 300 °C.

TPD and TPReaction were conducted using the same apparatus for Cu surface area measurements. For CO_2-TPD and H_2-TPD experiments, the catalysts (100-200 mg) were reduced in situ with 10% H_2/Ar at 250 °C for 2 h followed by purging with Ar for 30 min. Adsorption was subsequently conducted by exposing the reduced samples to CO_2 or 10% H_2/Ar at room temperature for 1 h followed by Ar purging for 30 min to remove physically adsorbed species. The catalyst temperature was increased from room temperature to 500 °C at a ramp rate of 10 °C/min under Ar. For TPReaction experiments, fresh catalysts were used for each reduction temperature. The catalysts (200 mg) were first reduced in a temperature range of 200-350 °C followed by cooling to room temperature. The reactor was then pressurized to 20 bar with a 25% CO_2/H_2 mixture (100 cm^3(STP)/min) and the catalyst temperature was raised linearly at the rate of 10 °C/min from room temperature to 500 °C. Fragments of the gas components in the outlet stream from the reactor were monitored using a ThermoStar mass spectrometer.

XRD patterns of the calcined catalysts were obtained with a PANalytical X'Pert Pro MPD diffractometer using Cu K_α radiation (λ = 1.542 Å) operated at 45 kV and 40 mA. XRD patterns were also recorded during in situ reduction under 4% H_2/N_2 (15 cm^3(STP)/min) by ramping at the rate of 10 °C/min with an isothermal soak for 2 h at every 50 °C increment up to 300 °C. Determination of copper crystallite size from Rietveld refinement was performed by

fitting the peaks in the XRD patterns after reduction at 250 °C using the pseudo-Voigt function (PVF) in X'Pert Highscore Plus software. The ZnO crystallite sizes of the same set of reduced samples were estimated from broadening of the ZnO(101) diffraction line using the Scherrer equation.

HRTEM and STEM images were obtained with a JEOL 2000 microscope. The catalysts were ultrasonically dispersed in ethanol and a few drops of the suspension were deposited on Si-nitride grids purchased from Ted-Pella, Inc. X-ray photoelectron spectroscopy (XPS) was performed using a PHI 5600ci instrument equipped with a monochromatic Al X-ray source ($h\nu$ = 1486.6 eV) operated at 400 W. The pass energy of the analyzer was set at 58.7 eV. In situ reduction at 250 °C was conducted in a separate reaction chamber that was attached directly to the XPS analysis chamber. The reduced samples were then transferred back to the analysis chamber without exposure to air. Peak binding energies were referenced to the Zn $2p_{3/2}$ peak located at 1021.1 eV.

DRIFTS experiments were performed using a Thermo Nicolet 4700 FTIR spectrometer equipped with an MCT detector and Smart Collector accessory for diffuse reflectance analysis. Catalysts diluted with KBr powder (5/95 w/w) and pure KBr were both loaded into sample cups inside a dual environmental chamber where thermocouples were mounted to directly measure the sample temperature. Spectra were averaged over 500 scans at a 4 cm^{-1} resolution in the mid IR range (400-4000 cm^{-1}). Background spectra were taken at different temperatures under He. The DRIFTS experimental conditions were the same as those used for CO_2-TPD. The catalysts were reduced in situ with 10% H_2/Ar at 250 °C for 2 h followed by purging with He for 30 min. CO_2 adsorption was conducted at room temperature for 1 h followed by He purging for 30 min. The spectra were subsequently collected upon heating in steps of 25 °C to 500 °C under He.

2.3 Activity Tests

Steady-state reaction experiments were performed using a fixed-bed flow reactor system (Process Integral Development Engineered & Tech., Spain) with a stainless steel tubular reactor (ID = 9.2 mm, L = 300 mm). The prepared catalysts were evaluated at 180-240 °C and 20 bar. The feed composition was $CO_2/H_2/N_2$ = 1/3/0.4 (total flow rate = 100 cm^3(STP)/min). The weight hourly space velocity (WHSV) was maintained at 0.03 $m^3/g_{cat}/h$ to ensure that the reaction conditions did not allow the system to approach the equilibrium-limited regime. Prior to reaction, the catalysts were reduced in situ with 10% H_2/N_2 (50 cm^3(STP)/min) at 250 °C and atmospheric pressure for 2 h. The feed and effluent streams were analyzed on-line using an automated Agilent GC 7890A equipped with FID and TCD detectors and a methanizer. Separation of components was performed using Ar as a carrier gas and 2 columns: Hayesep Q (10 ft x 1/8 in. SS, 80/100 mesh) and molecular sieve 13X (6 ft x 1/8 in. SS, 60/80 mesh). Reaction data were taken after 12 h of testing. The production rate of methanol is expressed in moles of methanol produced per kilogram Cu of the catalyst per hour. Percent methanol selectivity is defined as (moles of carbon in methanol)/(total moles of carbon in all carbon-containing products) x 100.

3 Results and Discussion

3.1 Catalyst Performance

Steady-state reaction experiments were conducted at equal WHSV to investigate the effect of reaction temperature on catalytic activity and product distributions. The rates of methanol production for various coprecipitated Cu/ZnO-based catalysts are compared in Figure 1a. Error bars are smaller than data points in this graph and are omitted from the figure for clarity. The

activity increases with reaction temperature from 180 to 240 °C for all the catalysts. Both CuZn and CuZnZr catalysts have comparable rates below 200 °C. Addition of Ga_2O_3 and/or Y_2O_3 in the CuZnZr catalyst formulation enhances the activity and the promotional effect is more evident at higher temperatures. At 240 °C, the activity increases in the following order: CuZn < CuZnZr < CuZnZrGa < CuZnZrY < CuZnZrGaY. Under the reaction conditions used in this study, the products from CO_2 hydrogenation are methanol, carbon monoxide, and water vapor. The selectivities of carbon-containing products obtained with the representative CuZnZrGaY catalyst are displayed in Figure 1b. As the reaction temperature is increased, methanol selectivity decreases whereas CO selectivity increases. These results indicate that the formation of CO via the reverse water-gas shift reaction ($CO_2 + H_2 \rightarrow CO + H_2O$) becomes more appreciable at higher temperatures, therefore leading to a decrease in methanol selectivity.

The trend in the catalytic activity shows a correlation to Cu surface area and the promotional effect of Ga_2O_3 and Y_2O_3. The best-performing CuZnZrGaY catalyst exhibits the largest Cu surface area among all the catalysts examined (Table 1). Previous work using Rietveld refinement of the XRD patterns showed that incorporating Ga_2O_3 and Y_2O_3 into the CuZnZr catalyst formulation caused a decrease of the average Cu crystallite size, which accounts for the increased Cu surface area and dispersion noted in Table 1 [9]. The ZnO phase has also been shown to be amorphous in the CuZnZrGa, CuZnZrY, and CuZnZrGaY catalysts, signaling that the sizes of the ZnO domains are below the XRD detection limit (i.e., < 3-5 nm) [9]. In addition, efficient catalysts demonstrate large Cu/Zn surface atomic ratio determined by XPS after reduction. The Cu/Zn surface ratio of the CuZnZrY and CuZnZrGaY catalysts is closer to the bulk value of 1.3 although all the ternary and multicomponent catalysts were prepared with the same Cu/Zn bulk ratio.

3.2 Adsorption Characteristics

TPD was carried out to determine the type and amount of adsorption sites for the reactant molecules (i.e., CO_2 and H_2) on the reduced catalysts. The TPD profiles of CO_2 (m/z = 44) after CO_2 adsorption at room temperature are shown in Figure 2a. The amount of CO_2 desorbed is quantified in Table 2. The corresponding profiles of Cu metal and pure ZnO are also included for comparison. Cu metal exhibits negligible CO_2 desorption as weakly adsorbed CO_2 is nearly completely removed after Ar flushing following an adsorption step. This finding is consistent with previous experiments on Cu films and single crystals [10] as well as polycrystalline Cu powders [11]. The amounts of CO_2 desorbed from the other oxide components (i.e., Ga_2O_3, Y_2O_3, and ZrO_2) are negligible under the same experimental conditions (not shown).

Pure ZnO exhibits higher CO_2 adsorption capacity than Cu metal as suggested by a much larger CO_2 desorption feature on ZnO in Figure 2a. The shape and location of the desorption feature seen with ZnO are in good accordance with ZnO supports prepared by Wang et al. [12]. Compared to ZnO, the CO_2 desorption feature at 80 °C over the CuZn catalyst grows larger and becomes less symmetrical with a tail extending up to 225 °C, suggesting that there are multiple types of adsorption sites with different binding strengths in this catalyst. Behrens et al. [13] recently demonstrated that Cu steps in close proximity to ZnO_x on the surface of industrial $Cu/ZnO/Al_2O_3$ catalysts were strong adsorption sites for oxygen-bound intermediates, consistent with the high temperature tail seen in our TPD results. Upon adding Ga_2O_3, Y_2O_3, and ZrO_2 in the CuZn catalyst, the CO_2 desorption feature grows larger while the peak maximum remains approximately at 80 °C, suggesting that these metal oxides enhance the number of the same type of CO_2 adsorption sites. Furthermore, the CO_2 desorption feature observed for the CuZnZrGaY catalyst is striking. There is an appreciable amount of CO_2 desorbing between 150 and 300 °C,

implying that these strongly adsorbed CO_2 species are expected to participate in the reaction by forming key intermediates via hydrogenation.

H_2-TPD was also conducted with the same set of the catalysts and the corresponding profiles (m/z = 2) are illustrated in Figure 2b. Pure ZnO is capable of chemisorbing H_2 as indicated by a small desorption feature at 270 °C. Negligible amounts of H_2 are desorbed from Cu metal and the other metal oxide components used as control experiments (not shown). Addition of Cu to ZnO creates a new H_2 desorption features at 80 °C and shifts the high temperature feature to ~ 320 °C. The amount of H_2 associated with the high-temperature feature also increases by nearly 20 fold (Table 2). Incorporation of Ga_2O_3, Y_2O_3, and ZrO_2 causes the low-temperature peak near 80 °C for the ternary and multicomponent catalysts to quantitatively decrease in intensity, broaden, and develop more sustained contributions at higher temperatures. The high-temperature feature near 320 °C quantitatively increases in intensity for the ternary and multicomponent catalysts. The amounts of H_2 desorbed below and above 150 °C have been determined and are shown in Table 2. Overall, the estimated desorption quantities are comparable to the values measured with CuZnZr catalysts by Arena et al. [14,15].

The appearance of the low-temperature feature with Cu addition, its decreasing intensity in the ternary and multicomponent catalysts, and the associated intensity increase of the high-temperature feature in these samples can be explained by a spillover effect with H_2 dissociating on Cu or at the interface with ZnO and H atoms binding directly to ZnO. Spillover has been seen in other systems when Cu and ZnO particles are finely dispersed and in intimate contact with each other [16,17]. Even physical mixing of Cu/SiO_2 and ZnO/SiO_2 catalysts has been shown to have higher methanol synthesis activity than their pure counterparts, suggesting that hydrogen spillover can take place between Cu and ZnO when the two phases are not in direct contact [17-

20]. It has been previously hypothesized that ZnO may act as a reservior by providing additional atomic hydrogen atoms via reverse spillover to facilitate the hydrogenation of carbonate and formate species adsorbed on Cu crystallites to form methanol [3,17,21-23].

Since pure ZnO has a high-temperature TPD feature at 270 °C, we attribute the 320 °C peak in the Cu-containing catalysts to associative recombination of H atoms and desorption from the ZnO. The nearly 20-fold increase of the intensity associated with the addition of Cu to ZnO would be consistent with the addition of a catalytic site capable of flooding the support with hydrogen and in line with a spillover interpretation of the TPD results. While it is difficult to precisely assign the adsorption site from these results, the ~50 °C shift in the peak maximum is interesting and possibly results from the modification of the ZnO domain sizes and defect structure. The decreasing size of the ZnO domains and their increasing amorphous nature have been demonstrated for these samples [9]. It is worth noting that H_2 adsorption on Cu surfaces is an activated process and this high-temperature feature has also been ascribed to the evolution of H_2 from subsurface layers of metallic Cu particles [24,25] and from bulk Cu when adsorption was performed above room temperature [26,27]. Since our adsorption was done at room temperature, it is unlikely that H_2 desorption from the subsurface layers or bulk Cu would appreciably contribute to the high-temperature feature seen in our TPD results. However, we cannot exclude the possibility of H_2 diffusing into subsurface layers and further into bulk Cu during a pre-reduction step at 250 ^{o}C prior to adsorption.

The low-temperature feature in the H_2-TPD profiles occurs at temperatures consistent with previous literature reports on dispersed and single-crystal Cu systems [24,28]. For example, Anger et al. [28] reported that the desorption peak maximum observed with three Cu surfaces (111), (110), and (100) depended on hydrogen coverage and ranged from ~0-100 °C. We

therefore assign the 80 °C feature in Figure 2b to associative H_2 desorption from metallic Cu and its interface with ZnO. The lower Cu content of the CuZnZrGa and CuZnZrGaY catalysts likely contributes to the decreased intensity of the low-temperature peak area. This finding agrees well with that reported by Duprez et al. [29] for coprecipitated CuZn catalysts containing similar Cu contents. The broadening of the low-temperature feature seen with the CuZnZrGa and CuZnZrGaY catalysts may result from higher binding energy sites which would be expected for the edge/defect sites, in relatively higher proportions than low-index planes in smaller Cu particles, such as those in the more complex catalyst compositions in Figure 2b [30].

DRIFTS coupled with TPD was performed to identify adsorbed species formed on the surface of pure ZnO and the CuZnZrGaY catalyst after CO_2 exposure at room temperature and examine their thermal stability during heating. Prior to CO_2 adsorption, there are already bands at 1532 and 1417 cm^{-1} as well as a shoulder at 1668 cm^{-1} seen at room temperature on the reduced CuZnZrGaY catalyst (Figure 3a). The band assignments are as follows: 1532 and 1417 cm^{-1}, symmetric stretching mode of monodentate carbonate species [31-33]; 1668 cm^{-1}, asymmetric stretching mode of bidentate carbonate or bicarbonate species [33-35]. As such, we assign these bands as being the result of leftover carbonates formed during the coprecipitation that were not completely removed after an air calcination step at 350 °C.

Upon CO_2 exposure, these main bands grow slightly in intensity and there are additional bands that are characteristic of monodentate and bidentate carbonate species seen at 1647 (strong), 1325 (weak shoulder), and 1208 (weak) cm^{-1}[33,34,36]. The sharpness of these features, particularly at 1647 cm^{-1} suggests that they arise from a surface bound carbonate species caused by the binding of CO_2 to the catalyst surface and differ from the species attributed to bulk carbonates seen prior to dosing. CO_2 is typically fairly unreactive with clean single

crystal Cu surfaces, but can form carbonate species on oxygen covered surfaces and with the metal oxides making up the support in the multicomponent catalyst (Figure 3a) [13,31-35,37]. The DRIFT spectra collected before and after CO_2 adsorption over pure ZnO are nearly identical and the spectrum of the CO_2-adsorbed sample is only shown for comparison.

Figure 3b displays a series of DRIFT spectra taken at various temperatures from room temperature to 500 °C after CO_2 adsorption on the reduced CuZnZrGaY catalyst. Upon heating in steps under He, the Cu-carbonate species start to decompose as the bands at 1647 and 1208 cm^{-1} and the weak shoulder at 1325 cm^{-1} decrease in intensity and disappear completely at 200 °C. The loss of leftover carbonates is consistent with a marked intensity decrease of the main bands at 1532 and 1417 cm^{-1} and an appearance of the valley near 1647 cm^{-1} at higher temperatures. Eventually, the separation between the bands at 1532 and 1417 cm^{-1} becomes less distinct, resulting in one large band at 500 °C. Millar et al. [32] demonstrated that interfacial bidentate carbonates species were formed at 1615 cm^{-1} on the surface of a reduced $Cu/ZnO/SiO_2$ catalyst after CO_2 adsorption at room temperature. However, we do not have conclusive spectroscopic evidence for adsorption sites located at the Cu-ZnO interfaces due to a large amount of leftover carbonates in the CuZnZrGaY catalyst. In an attempt to relate the bands at 1647 and 1208 cm^{-1} to the CO_2 desorption features previously observed in the TPD profiles, a control experiment was conducted by exposing the reduced CuZnZrGaY catalyst to the same temperature program without a CO_2 adsorption step. Apparently, the low-temperature desorption feature at 80 °C is missing in the TPD profile of the catalyst without preadsorbed CO_2 (Figure 3b, inset). These results substantiate that the 80 °C feature is mainly attributed to CO_2 desorption from metallic Cu sites and the high-temperature feature at 330 °C corresponds to the decomposition of leftover carbonates.

3.3 Deactivation Characteristics

It is well known that Cu sintering is the primary cause of deactivation in Cu/ZnO-based methanol synthesis catalysts [5,6,38,39]. Sintering is a highly temperature-dependent process and its underlying mechanism is surface diffusion of a monomer dispersion or small clusters of atoms [4,40-42]. The temperatures at which atoms at defects and from the bulk become mobile are the Hüttig and Tamman temperatures, respectively ($T_{Hüttig} = 0.3T_{melting}$, $T_{Tamman} = 0.5T_{melting}$) where the melting point temperature is 1083 °C for Cu and is 1975 °C for ZnO. However, sintering can sometimes occurs at temperatures far below the Tamman temperature depending on several factors including catalyst properties and pretreatment/reaction conditions [43]. In commercial catalyst formulations, ZnO acts as a physical spacer rather than as a support because ZnO particles appear in similar or even smaller sizes compared to Cu particles [23]. The tendency for sintering depends on the interaction between Cu and ZnO via epitaxial or electronic bonding [8,44]. The growth of ZnO particles weakens the Cu-ZnO interfacial contact, thereby leading to the agglomeration of Cu particles. Matsumura et al. [45] discovered the concomitant increase of Cu and ZnO particle sizes for deactivated catalysts after exposure to methanol steam reforming conditions. Topsoe and coworkers [46] demonstrated that the dynamic shape changes of Cu nanocrystals dispersed on ZnO was attributed to changes in the Cu/ZnO interface energy and this finding was not observed with silica-supported samples. Surface science and computational studies have provided supporting evidence that ZnO substrate stabilized the growth of Cu clusters in model catalysts [47-49]. Accordingly, ZnO plays a crucial role in dispersing Cu particles and stabilizing them against sintering. It is desirable to produce ZnO in a finely divided state to prevent Cu sintering. Parameters affecting the crystallinity, morphology, and particle size of ZnO will have a strong impact on the Cu dispersion and, in turn, on catalyst

performance. In this study, textural promoters (i.e, Ga_2O_3 and Y_2O_3) are introduced during synthesis to aid in delaying the crystallization of ZnO particles and maintaining their nanosize under reduction and reaction conditions. We have examined the effect of reduction temperature on the sintering behavior of the most active (CuZn) and least active (CuZnZrGaY) catalysts using a variety of in situ and ex situ characterization techniques.

In situ XRD was conducted to investigate crystallinity and crystal phase transformations of the CuZn and CuZnZrGaY catalysts during reduction with flowing 4% H_2/Ar from room temperature to 300 °C. The calcined CuZn catalyst is crystalline as demonstrated by the presence of strong diffraction peaks associated with crystalline CuO and ZnO phases (Figure 4a). As the reduction temperature is increased, the CuO(111) peak at 38.7° decreases in intensity and disappears completely at 200 °C with the concomitant appearance of Cu(111), Cu(200), and Cu(220) peaks at 43.1°, 50.1°, 73.7°, respectively. Under these experimental conditions, bulk crystalline CuO undergoes a complete reduction at 200 °C to metallic Cu, which is an active phase for CO_2 hydrogenation to methanol [9]. Cu metal and ZnO peaks grow sharper at higher temperatures up to 300 °C, suggesting that both Cu and ZnO particles continue to sinter. In contrast, the calcined CuZnZrGaY catalyst does not possess long-range order to diffract X-rays and is therefore amorphous. This finding is supported by a broad peak around 32-34° in Figure 4b. The CuZnZrGaY catalyst is resistant to Cu sintering as indicated by the Cu(111) peak, which is much broader and maintains its intensity throughout the experiment. Rietveld analysis on the XRD patterns collected separately after in situ reduction at 250 °C have confirmed that the average Cu crystallite diameter is 19 nm for the CuZn catalyst and is 9 nm for the CuZnZrGaY catalyst (Table 1). There are no separate crystalline phases containing the other oxide components (particularly ZnO) observed with the CuZnZrGaY catalyst, suggesting that these

metal oxides remain either amorphous or well-dispersed during reduction. Thus, improved Cu sintering resistance is related to the transformation of the highly crystalline ZnO phase to an amorphous structure upon Ga and Y promotion.

ZnO particles containing Ga_2O_3 or Y_2O_3 were then prepared in the same manner as the Cu/ZnO-based catalysts to corroborate the promotional effect of Ga_2O_3 and Y_2O_3 on sintering resistance. As displayed in Figure 4c, pure ZnO is highly crystalline with a hexagonal wurtzite structure [50]. The introduction of Ga_2O_3 or Y_2O_3 is effective in hindering the growth of ZnO crystallites during synthesis as evidenced by broader and overlapping ZnO diffraction peaks in the patterns obtained with the Ga- and Y-doped samples. Brehm et al. [50] reported that doping with small amounts of Ga (e.g., 2-3 at%) decreased the ZnO grain size due to the incorporation of Ga on interstitial sites in the wurtzite crystal structure. The crystallinity and crystal planes of ZnO are verified by TEM images and their corresponding selected area electron diffraction (SAED) patterns (Figure 5). As expected, the SAED pattern of pure ZnO displays a series of distinct concentric rings which are indexed to wurtzite ZnO with crystal planes matching those previously identified by XRD. The SAED pattern for the Y-doped sample consists of broad and diffuse rings without visible diffraction spots, indicative of a much finer grain size for ZnO in this sample. Conceivably, Ga_2O_3 and Y_2O_3 provide a barrier to coalescence by preventing neighboring ZnO particles from diffusing together, thereby assisting ZnO in stabilizing Cu particles more effectively.

To characterize the bulk composition and morphology of particles in the CuZn and CuZnZrGaY catalysts after 250 °C reduction, cross-sectional TEM samples were prepared and subsequent STEM imaging and localized compositional analysis were performed using energy dispersive X-ray analysis. Metallic Cu aggregates display bright contrast relative to the ZnO

matrix in the CuZn catalyst (Figure 6a). There is no clear evidence of Cu enrichment from a STEM image collected with the CuZnZrGaY catalyst as particles are much smaller and are homogeneously dispersed. The corresponding atomic concentrations of all the elements are listed in Table 3 and a composition variation is observed between the regions that were examined in both catalysts. For the CuZn catalyst, a significant spatial variation of Cu content is observed due to the relatively large particle size. The Cu content of the CuZnZrGaY catalyst is much more homogeneous and is consistent with the bulk value determined by ICP-OES. The data presented in Table 3 suggest that the distribution of the Ga promoter is not homogeneous in the multicomponent catalyst. The measured d-spacings in HRTEM images provide information about the crystal phase of individual particles and can be used to distinguish between Cu and ZnO particles. The grain sizes of ZnO particles in the CuZn catalyst vary and range from 10 nm in diameter to much larger. A representative HRTEM image of a ZnO nanorod seen with the CuZn catalyst is displayed in Figure 6b. For the CuZnZrGaY catalyst, a large number of spherical crystals of ~2-4 nm in size are indexed to the ZnO(100) crystallographic plane (d-spacing = 0.29 nm) and they are in intimate contact with larger Cu crystallites of ~10 nm in size. These Cu crystals exhibit a d-spacing of ~0.2 nm, which is consistent with face-centered cubic (fcc) Cu(111). The average Cu and ZnO particle sizes obtained from TEM agree well with the estimates from in situ XRD. Small ZnO particles of 2-4 nm in size are well-dispersed in the CuZnZrGaY catalyst and are not detectable by XRD. Moreover, an intimate contact between Cu and ZnO particles not only suppresses the Cu sintering but also enhances the CO_2 and H_2 adsorption capacities of the CuZnZrGaY catalyst probably due to the presence of additional sites created at the Cu-ZnO interfaces. This TEM observation is consistent with the explanations of the TPD results. After 12-h reaction, agglomerated particles with a branch-like structure are

formed in the CuZn catalyst whereas the particles in the spent CuZnZrGaY catalyst remains homogeneously distributed (Figure 6c). The differences in the ZnO morphology and particle size as well as varying degree of ZnO crystallinity are responsible for the observed variations in Cu dispersion (Table 1).

Reduction temperature is a key parameter that controls Cu crystallite size, which ultimately determines the performance of Cu/ZnO-based catalysts. Relative change in Cu dispersion as a function of reduction temperature can be used to assess catalyst stability. In an effort to measure the extent of Cu sintering, N_2O decomposition and TPR were conducted consecutively after in situ reduction with 10% H_2/Ar. Figure 7 illustrates relative Cu dispersion values of the CuZn and CuZnZrGaY catalysts at different reduction temperatures ranging between 200 and 300 °C. Relative dispersion is defined as the ratio of Cu dispersion measured at a specified reduction temperature to that measured at 200 °C. The CuZn catalyst shows a continuous decrease in Cu dispersion with reduction temperature and loses approximately 30% of its original dispersion after 300 °C reduction. On the other hand, the CuZnZrGaY catalyst exhibits only 6% loss of dispersion at 225 °C and remains relatively stable at higher reduction temperatures.

TPReaction was conducted to examine the effect of reduction temperature on catalytic activity by exposing the catalysts that are pre-reduced in situ to a linear temperature program under a flow of 25% CO_2/H_2 at 20 bar. In this experiment, the activity loss is defined as follows: $[(A_{200°C} - A_T) / A_{200°C}] \times 100$ where $A_{200°C}$ and A_T are areas under the methanol peak (m/z = 31) for the reduction temperature of 200 °C and above (i.e, 250, 300, and 350 °C), respectively. In most cases, the methanol signal starts to rise at approximately 170 °C, reaches a maximum between 265 and 280 °C, and then decreases to the starting value around 400 °C (Figure 8). For

the CuZnZrGaY catalyst, the shape and location of the methanol peak are slightly affected by the reduction temperature. However, the methanol peak maximum over the CuZn catalyst shifts to a higher temperature by 60 °C when the reduction temperature is raised to 350 °C, indicative of severe Cu sintering. Although both catalysts exhibit the activity loss, the CuZnZrGaY catalyst remains more active than the CuZn catalyst at all reduction temperatures based on the methanol peak area (Figure 8, inset). The CuZn catalyst loses over half of its original activity at 350 °C while the CuZnZrGaY catalyst is relatively stable. The trend for the activity loss is consistent with the observed changes in the relative Cu dispersion. All in all, Cu sintering contributes to the deactivation of Cu/ZnO-based methanol synthesis catalysts and can be minimized greatly by incorporating Ga_2O_3 and Y_2O_3 to assist ZnO in stabilizing Cu crystallites.

4 Conclusions

The crystallinity, morphology, and particle size of ZnO have a strong impact on the performance of coprecipitated Cu/ZnO-based catalysts for methanol synthesis from CO_2 hydrogenation. The incorporation of Ga_2O_3 and Y_2O_3 as textural promoters delays the crystallization of ZnO during synthesis and produces an amorphous-like structure. The catalysts containing amorphous ZnO exhibit significantly higher activity and stability than their counterparts with crystalline ZnO. The synergy between Cu and ZnO may be associated with an intimate contact between the two components, which creates additional adsorption sites for CO_2 and H_2. A large amount of spherical ZnO nanoparticles with sizes of ~2-4 nm are found in the Ga and Y-promoted catalysts and they aid in preventing Cu particles from agglomeration during exposure to the pretreatment and reaction conditions. ZnO is an essential component because it acts as a hydrogen reservior for methanol synthesis on Cu crystallites and stabilizes them against sintering.

Acknowledgments As part of the National Energy Technology Laboratory's Regional University Alliance (NETL-RUA), a collaborative initiative of the NETL, this technical effort was performed under the RES contract DE-FE-0004000. This project was funded by the Department of Energy, National Energy Technology Laboratory, an agency of the United States Government, through a support contract with URS Energy & Construction, Inc. Neither the United States Government nor any agency thereof, nor any of their employees, nor URS Energy & Construction, Inc., nor any of their employees, makes any warranty, expressed or implied, or assumes any legal liability or responsibility for the accuracy, completeness, or usefulness of any information, apparatus, product, or process disclosed, or represents that its use would not infringe privately owned rights. Reference herein to any specific commercial product, process, or service by trade name, trademark, manufacturer, or otherwise, does not necessarily constitute or imply its endorsement, recommendation, or favoring by the United States Government or any agency thereof. The views and opinions of authors expressed herein do not necessarily state or reflect those of the United States Government or any agency thereof.

References

1. Saito M (1998) Catal Surv Jpn 2: 175-184
2. Wang W, Wang S, Ma X, Gong J (2011) Chem Soc Rev 40: 3703-3727
3. Liu XM, Lu GQ, Yan ZF, Beltramini J (2003) Ind Eng Chem Res 42: 6518-6530
4. Bartholomew CH (2001) Appl Catal A 2001: 17-60
5. Twigg MV, Spencer MS (2003) Top Catal 22: 191-203
6. Kung HK (1992) Catal Today 11: 443-453
7. Spencer MS (1998) Catal Lett 50: 37-40
8. Spencer MS (1999) Top Catal 8: 259-266
9. Natesakhawat S, Lekse JW, Baltrus JP, Ohodnicki PR, Howard BH, Deng X, Matranga C (2012) ACS Catal 2: 1667-1676
10. Solymosi F (1991) J Mol Catal 65: 337-358
11. Hadden RA, Vandervell HD, Waugh KC, Webb G (1988) Catal Lett 1: 27-34
12. Wang J, Luo L (2008) Catal Lett 126: 325-332

13. Behrens M, Studt F, Kasatkin I, Kuhl S, Havecker M, Abild-Pedersen F, Zander S, Girgsdies F, Kurr P, Kniep BL, Tovar M, Fischer RW, Norskov JW, Schlogl R (2012) Science 336: 893-897
14. Arena F, Italiano G, Barbera K, Bordiga S, Bonura G, Spadaro L, Frusteri F (2008) Appl Catal A 350: 16-23
15. Arena F, Italiano G, Barbera K, Bonura G, Spadaro L, Frusteri F (2009) Catal Today 143: 80-85
16. Millar GJ, Rochester CH, Bailey S, Waugh KC (1992) J Chem Soc Faraday Trans 88: 2085-2093
17. Burch R, Golunski SE, Spencer MS (1990) J Chem Soc Faraday Trans 86: 2683-2691
18. Burch R, Chappell RJ, Golunski SE (1988) Catal Lett 1: 439-444
19. Burch R, Chappell RJ (1988) Appl Catal 45: 131-150
20. Burch R, Chappell RJ, Golunski SE (1989) J Chem Soc Faraday Trans 85: 3569-3578
21. Connor WC, Falconer JL (1995) Chem Rev 95: 759-788
22. Prins R (2012) Chem Rev 112: 2714-2738
23. Kasatkin I, Kurr P, Kniep N, Trunschke A, Schlogl R (2007) Angew Chem Int Ed 46: 7324-7327
24. Tabatabaei J, Sakakini BH, Watson MJ, Waugh KC (1999) Catal Lett 59: 143
25. Wilmer H, Genger T, Hinrichsen O (2003) J Catal 215: 188-198
26. Rasmussen PB, Holmblad PM, Christoffersen H, Taylor PA, Chorkendorff I (1993) Surf Sci 287: 79-83
27. Genger T, Hinrichsen O, Muhler M (1999) Catal Lett 59: 137-141
28. Anger G, Winkler A, Rendulic KD (1989) Surf Sci 220: 1-17
29. Duprez D, Barbier J, Hamida ZF, Bettahar M (1984) Appl Catal 12: 219-225
30. Muhler M, Nielsen LP, Tornqvist E, Clausen BS, Topsoe H (1992) Catal Lett 14: 241-249
31. Koeppel RA, Baiker A, Schild C, Wokaun A (1991) J Chem Soc Faraday Trans 87: 2821-2828
32. Millar GJ, Rochester CH (1993) J Chem Soc Faraday Trans 89: 1109-1115
33. Bianchi D, Chafik T, Khalfallah M, Teichner SJ (1993) Appl Catal A 105: 223-249
34. Schild C, Wokaun A, Baiker A (1990) J Mol Catal 63: 243-254
35. Collins SE, Baltanas MA, Bonvardi AL (2004) J Catal 226: 410-421
36. Edwards JF, Schrader GL (1985) J Phys Chem 89: 782-788
37. Grabow LC, Mavrikakis M (2011) ACS Catal. 1: 365-384
38. Twigg MV, Spencer MS (2001) Appl Catal A 212: 161-174
39. Sun JT, Metcalfe IS, Sahibzada M (1999) Ind Eng Chem Res 38: 3868-3872
40. Moulijn JA, Diepen AEv, Kapteijn F (2001) Appl Catal A 212: 3-16
41. Campbell CT, Parker SC, Starr DE (2002) Science 298: 811-813
42. Wanke SE, Flynn PC (1975) Catal Rev Sci Eng 12: 93-135
43. Bartholomew CH (1993) Appl Catal A 107: 1-57
44. Kurr P, Kasatkin I, Girgsdies F, Trunschke A, Schlögl R, Ressler T (2008) Appl Catal A 348: 153-164
45. Matsumura Y, Ishibe H (2009) Appl Catal B 91: 524-532
46. Hansen PL, Wagner JB, Helveg S, Rostrup-Nielsen JR, Clausen BS, Topsoe H (2002) Science 295: 2053-2055
47. Koplitz LV, Dulub O, Diebold U (2003) J Phys Chem B 107: 10583-10590
48. Dulub O, Batzill M, Diebold U (2005) Top Catal 36: 65-76

49. French SA, Sokol AA, Catlow CRA, Sherwood P (2008) J Phys Chem C 112: 7420-7430
50. Brehm JU, Winterer M, Hahn H (2006) J Appl Phys 100: 064311-9

Figure Captions

Fig. 1 Effect of reaction temperature: (a) methanol production rate (b) product selectivities

Fig. 2 (a) CO_2-TPD profiles (b) H_2-TPD profiles

Fig. 3 (a) Comparison of DRIFT spectra taken before and after CO_2 adsorption on pure ZnO and the CuZnZrGaY catalyst (b) DRIFTS spectra for CO_2-TPD over the CuZnZrGaY catalyst (an inset compares CO_2-TPD profiles obtained with and without CO_2 adsorption)

Fig. 4 XRD patterns: in situ reduction of (a) CuZn and (b) CuZnZrGaY; (c) ex situ calcination of ZnO samples

Fig. 5 TEM image and corresponding SAED pattern: (a) ZnO (b) ZnO-Y_2O_3

Fig. 6 (a) STEM images of the reduced catalysts (b) HRTEM images of the reduced catalysts; insets show ZnO zone axis (ZA) orientation (c) TEM images of the spent catalysts

Fig. 7 Relative Cu dispersion as a function of reduction temperature

Fig. 8 Comparison of the methanol signal obtained during TPReaction at various reduction temperatures (an inset displays activity loss for the CuZn and CuZnZrGaY catalysts)

Table 1 Characteristics of prepared Cu/ZnO-based catalysts

Catalyst[a]	S_{BET} (m^2/g)		S_{Cu} (m^2/g_{Cu})	$\%D_{Cu}$	d_{XRD} (nm)		Cu/Zn XPS ratio
	Calcined	Reduced			Cu	ZnO	
CuZn (41/59)	65	56	41.7	6.5	19.4	11.5	0.299
CuZnZr (45/31/24)	126	105	43.5	6.7	13.2	8.6	0.452
CuZnZrGa (39/29/21/11)	143	139	57.1	8.9	12.7	<3-5[b]	0.591
CuZnZrY (37/27/21/15)	96	91	74.8	11.6	9.2	<3-5[b]	1.195
CuZnZrGaY (35/24/19/9/13)	125	110	94.4	14.6	9.0	<3-5[b]	1.143

[a] The numbers in parentheses are actual metal contents in mol% determined by ICP-OES.
[b] Below the XRD detection limit.

Table 2 TPD results

Catalyst	CO_2 desorbed (T ≈ 80 °C)		H_2 desorbed (T < 150 °C)		H_2 desorbed (T > 150 °C)	
	μmol/g	μmol/m^2	μmol/g	μmol/m^2	μmol/g	μmol/m^2
Cu	7	0.33	0	0.00	0	0.00
ZnO	31	0.76	0	0.00	3	0.08
CuZn	58	1.04	217	0.77	51	0.90
CuZnZr	138	1.31	90	0.17	99	0.94
CuZnZrGa	154	1.11	90	0.13	125	0.90
CuZnZrGaY	202	1.84	88	0.16	157	1.43

Table 3 EDX results for the catalysts reduced at 250 ^{o}C

Catalyst	Atomic concentration (%)				
	Cu	Zn	Zr	Ga	Y
CuZn					
Region 1	65.4	34.6			
Region 2	76.8	23.2			
Region 3	17.2	82.8			
Region 4	54.5	45.5			
ICP-OES	41.0	59.0			
CuZnZrGaY					
Region 1	33.1	19.8	29.4	3.7	14.0
Region 2	31.3	24.4	13.5	19.5	11.3
Region 3	41.1	19.1	19.5	4.8	15.5
Region 4	27.5	15.2	32.9	6.2	18.2
Region 5	38.5	15.5	26.0	0.5	19.5
ICP-OES	35.0	24.0	19.0	9.0	13.0

Fig. 1

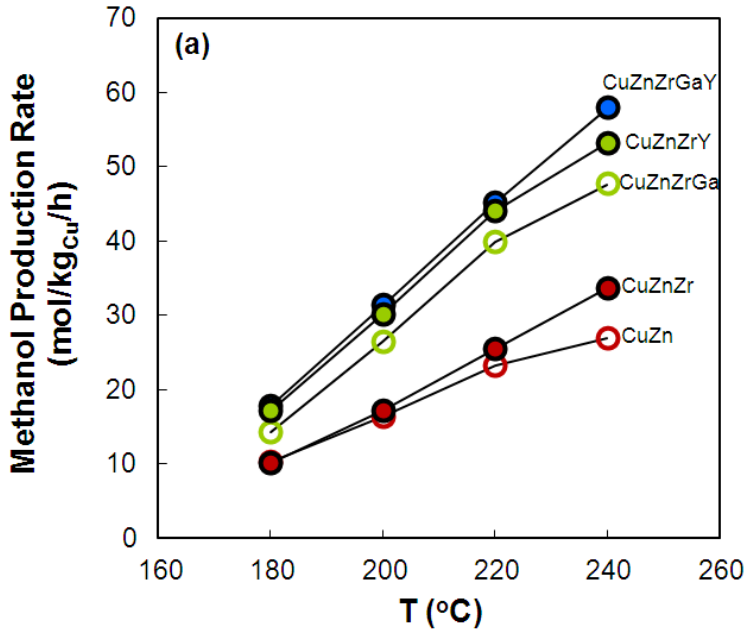
(a)
Methanol Production Rate
(mol/kgCu/h)
T (°C)
CuZnZrGaY
CuZnZrY
CuZnZrGa
CuZnZr
CuZn
0
10
20
30
40
50
60
70
160
180
200
220
240
260

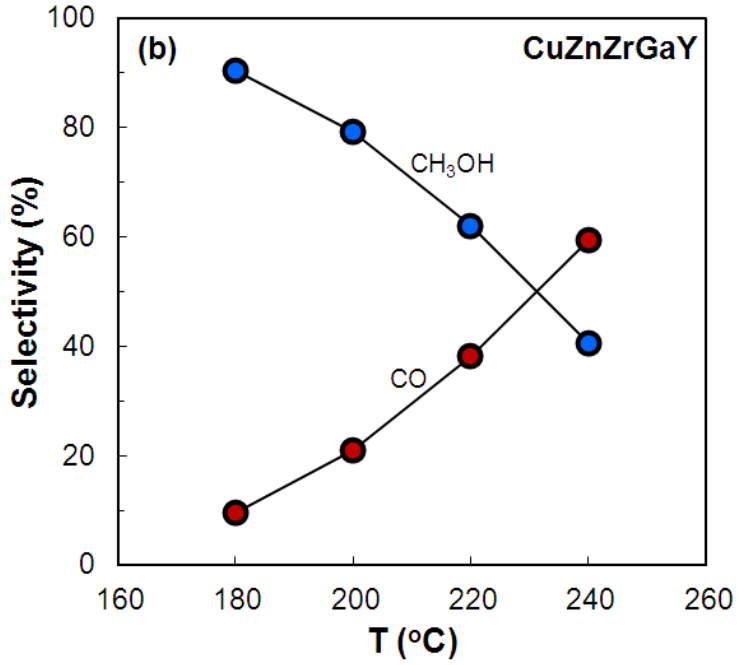
(b)
CuZnZrGaY
Selectivity (%)
T (°C)
CH3OH
CO
0
20
40
60
80
100
160
180
200
220
240
260

Fig. 2

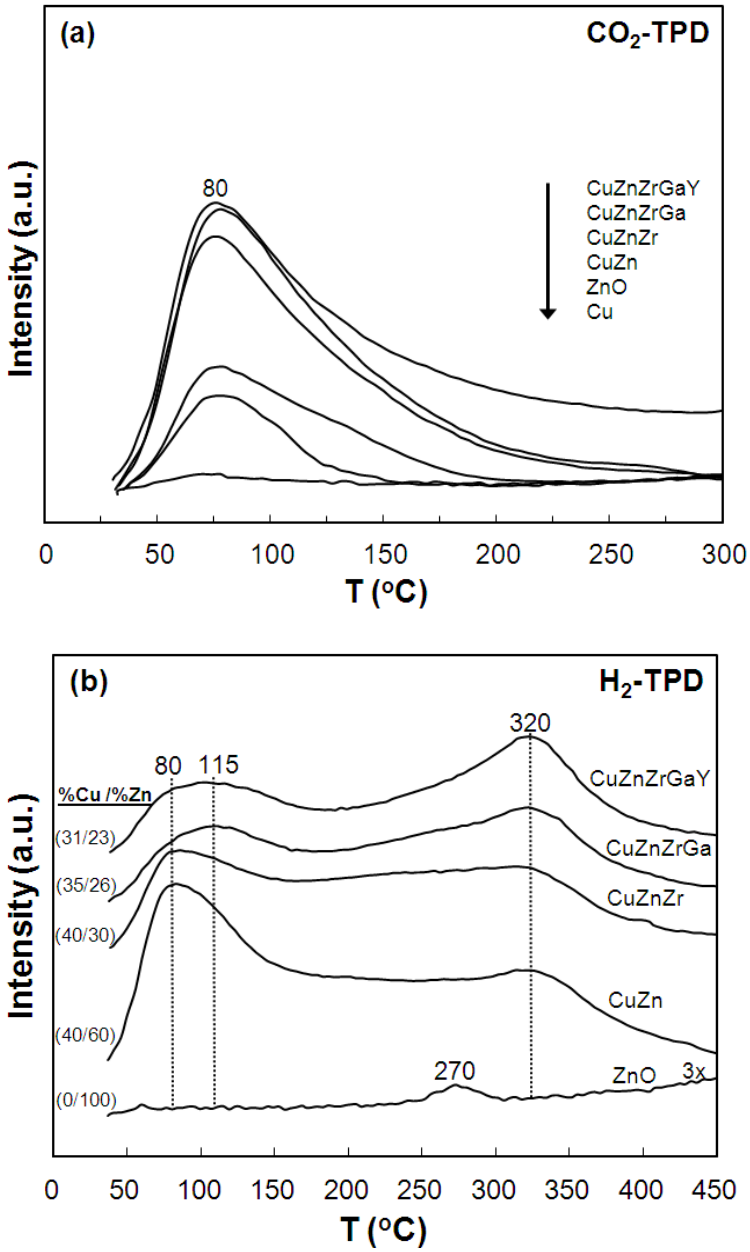
(a)
CO_2-TPD
Intensity (a.u.)
80
CuZnZrGaY
CuZnZrGa
CuZnZr
CuZn
ZnO
Cu
0
50
100
150
200
250
300
T (°C)
(b)
H_2-TPD
Intensity (a.u.)
320
80
115
%Cu /%Zn
(31/23)
(35/26)
(40/30)
(40/60)
(0/100)
CuZnZrGaY
CuZnZrGa
CuZnZr
CuZn
270
ZnO
3x
0
50
100
150
200
250
300
350
400
450
T (°C)

Fig. 3

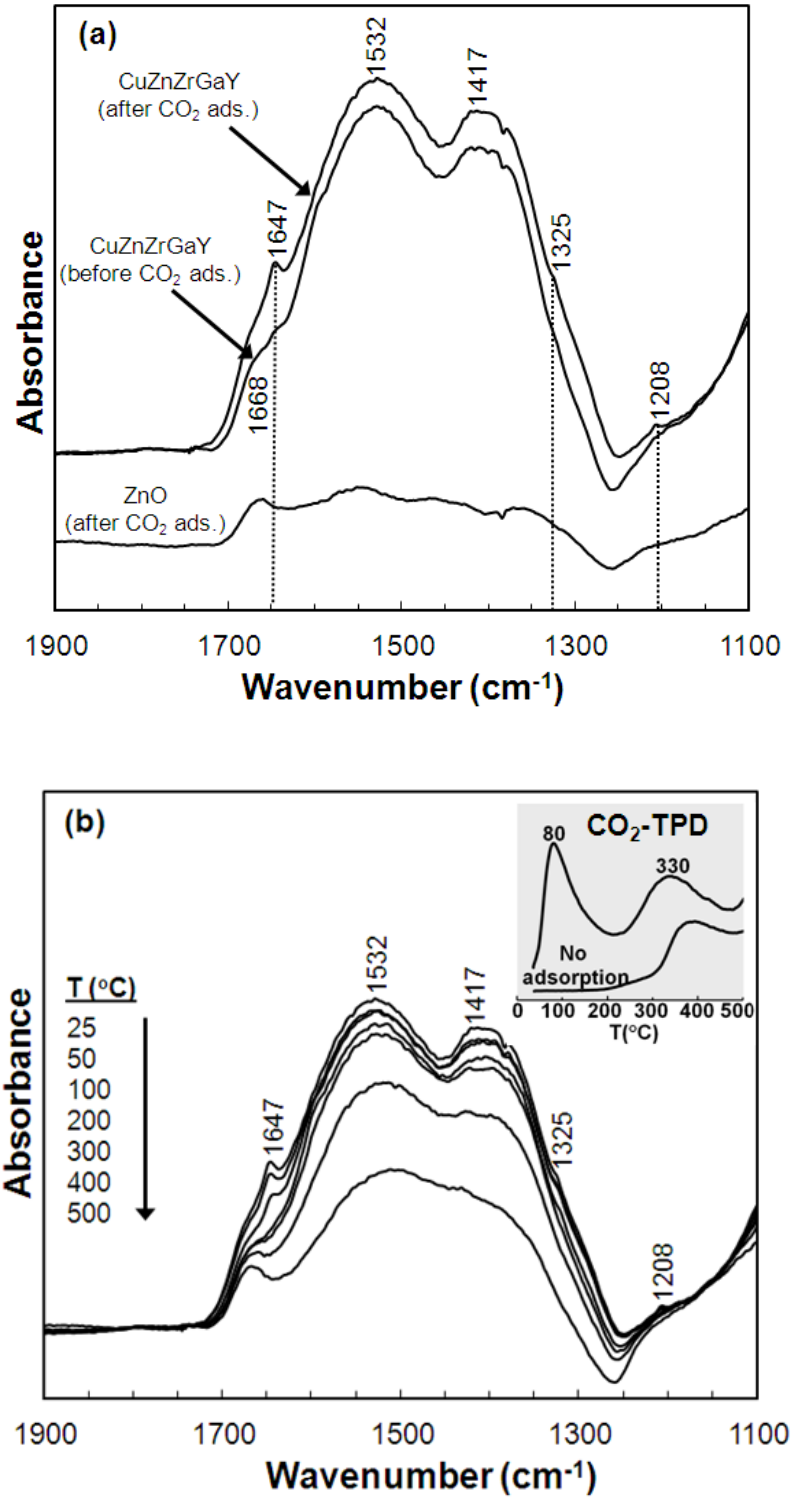
(a)
CuZnZrGaY
(after CO_2 ads.)
CuZnZrGaY
(before CO_2 ads.)
ZnO
(after CO_2 ads.)
1532
1417
1647
1325
1668
1208
Absorbance
1900
1700
1500
1300
1100
Wavenumber (cm^{-1})
(b)
CO_2-TPD
80
330
No
adsorption
0 100 200 300 400 500
T(°C)
T (°C)
25
50
100
200
300
400
500
1532
1417
1647
1325
1208
Absorbance
1900
1700
1500
1300
1100
Wavenumber (cm^{-1})

Fig. 4

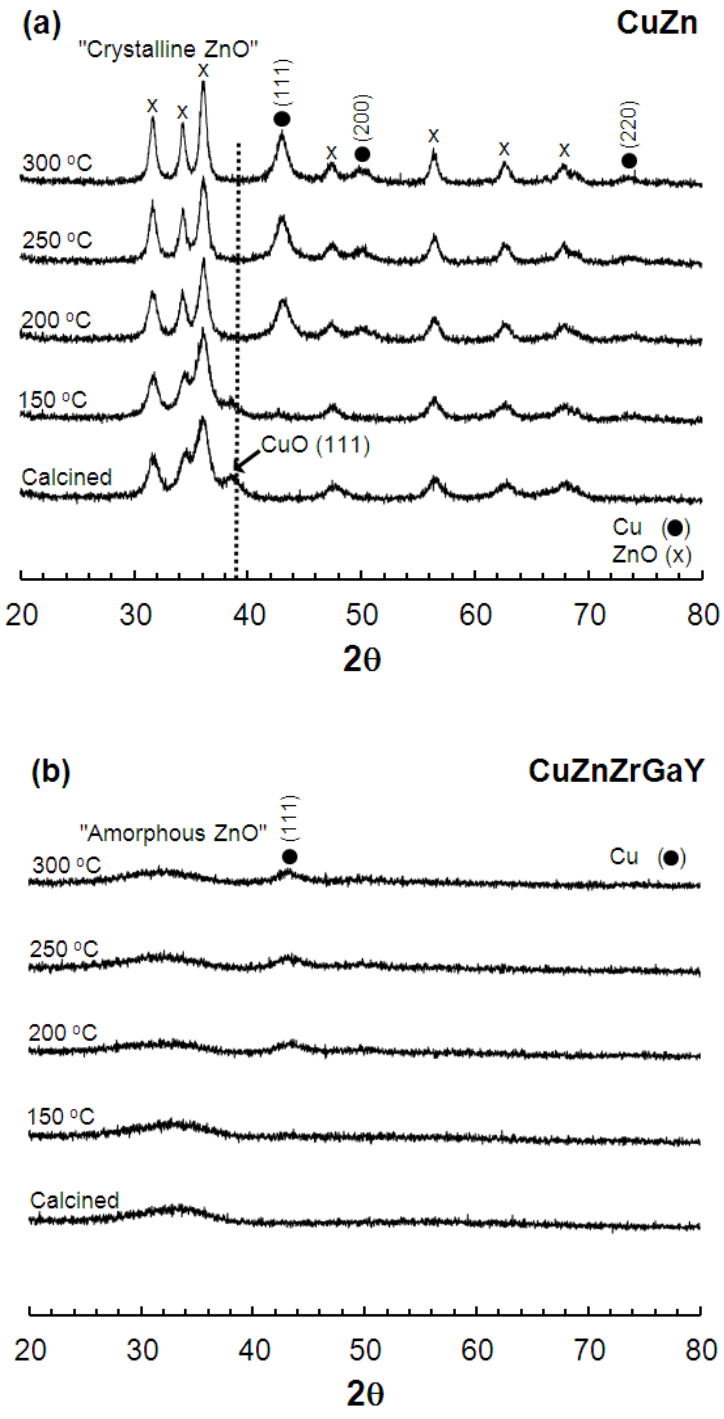
(a)
CuZn
"Crystalline ZnO"
(111)
(200)
(220)
300 °C
250 °C
200 °C
150 °C
Calcined
CuO (111)
Cu (●)
ZnO (x)
20
30
40
50
60
70
80
2θ
(b)
CuZnZrGaY
"Amorphous ZnO"
(111)
Cu (●)
300 °C
250 °C
200 °C
150 °C
Calcined
20
30
40
50
60
70
80
2θ

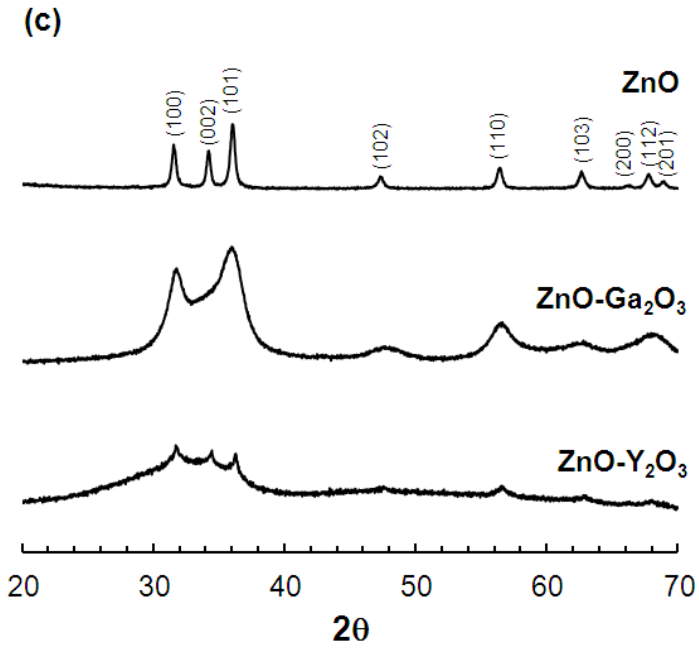
(c)
ZnO
(100)
(002)
(101)
(102)
(110)
(103)
(200)
(112)
(201)
ZnO-Ga2O3
ZnO-Y2O3
20
30
40
50
60
70
2θ

Fig. 5

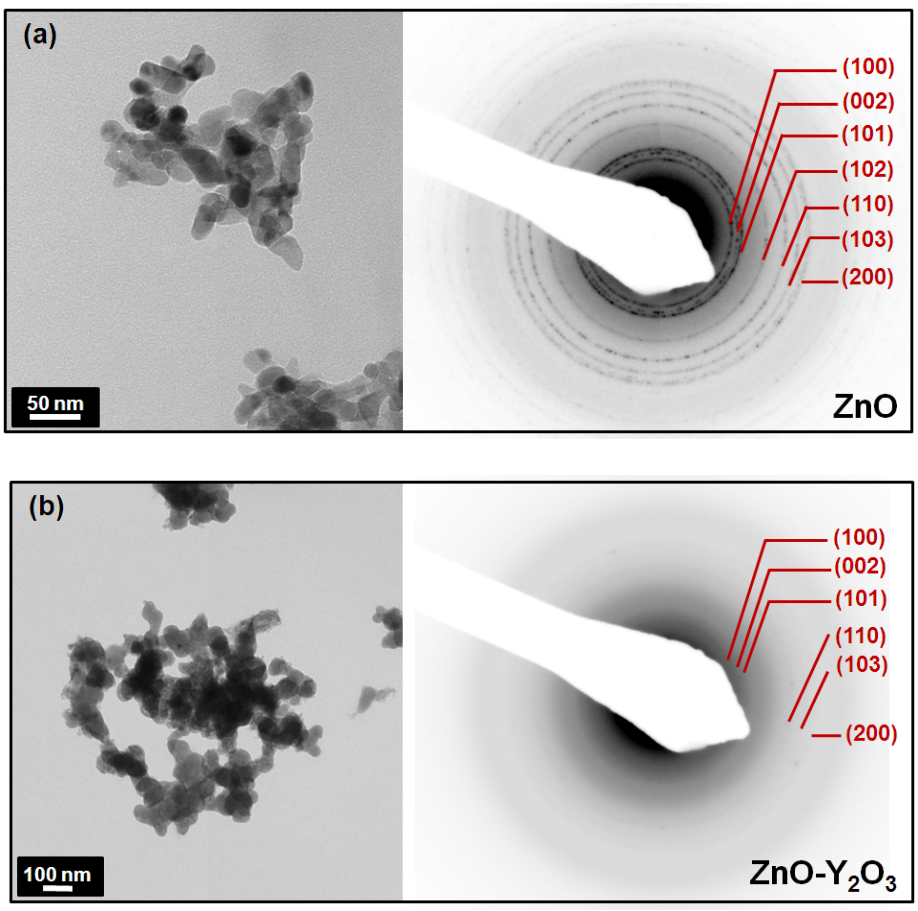
(a)
50 nm
(100)
(002)
(101)
(102)
(110)
(103)
(200)
ZnO
(b)
100 nm
(100)
(002)
(101)
(110)
(103)
(200)
ZnO-Y2O3

Fig. 6

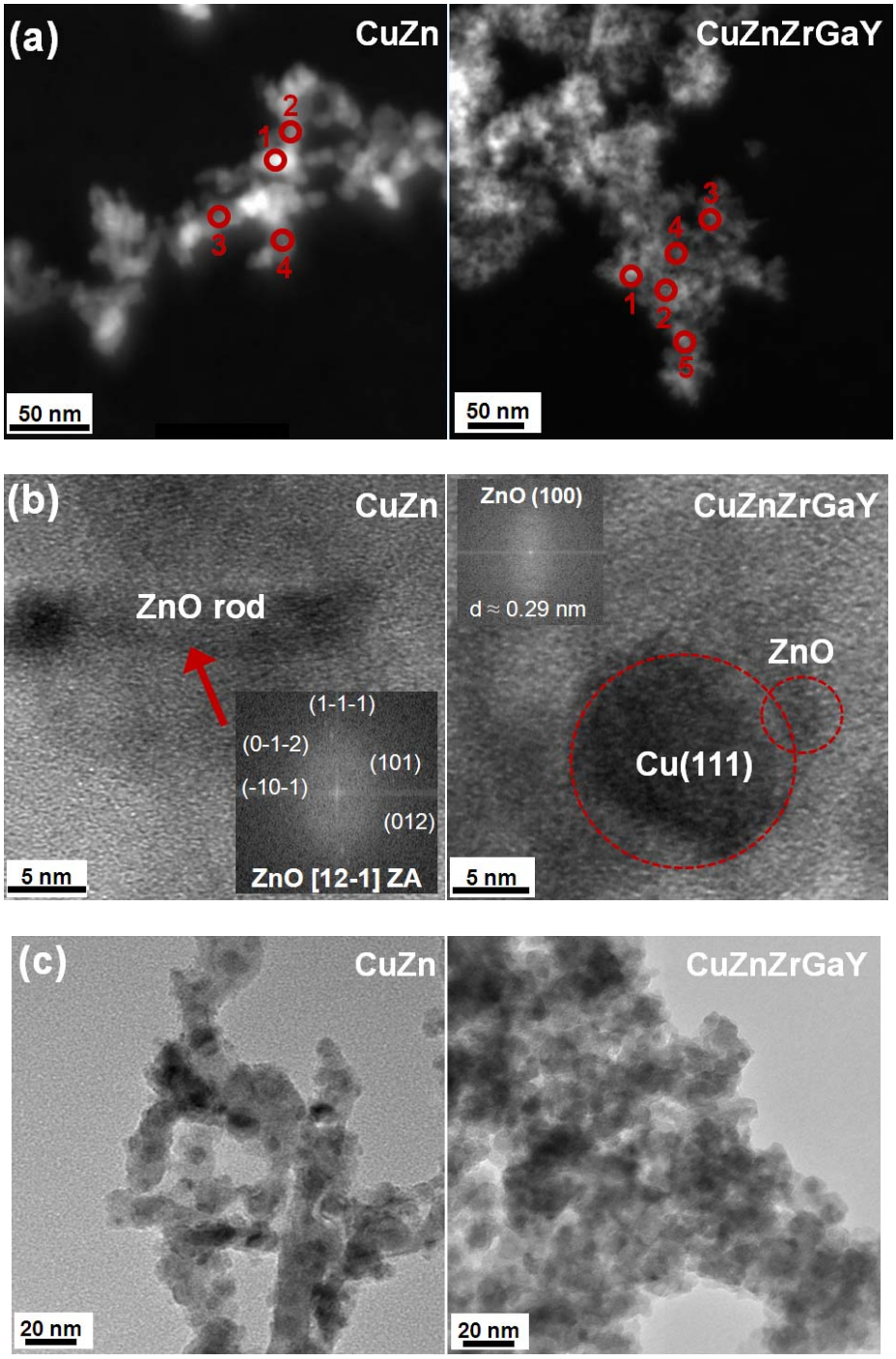
(a)
CuZn
1
2
3
4
50 nm
CuZnZrGaY
1
2
3
4
5
50 nm
(b)
CuZn
ZnO rod
(1-1-1)
(0-1-2)
(101)
(-10-1)
(012)
ZnO [12-1] ZA
5 nm
ZnO (100)
d ≈ 0.29 nm
CuZnZrGaY
ZnO
Cu(111)
5 nm
(c)
CuZn
20 nm
CuZnZrGaY
20 nm

Fig. 7

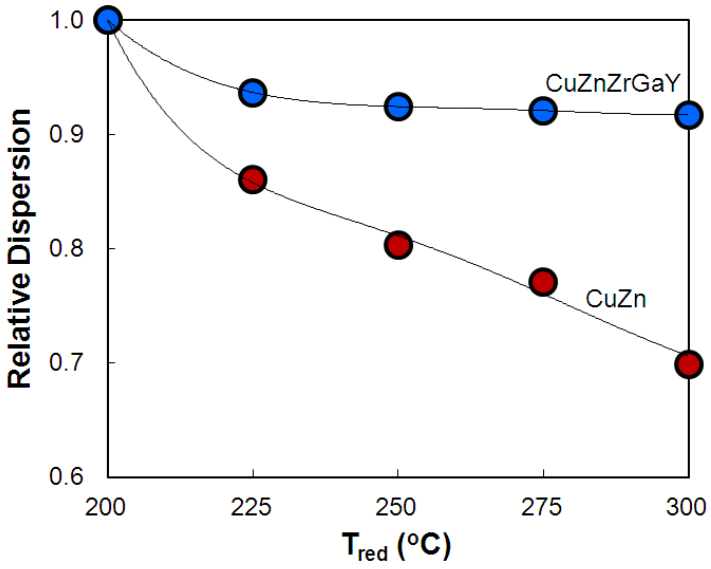
1.0
0.9
0.8
0.7
0.6
Relative Dispersion
CuZnZrGaY
CuZn
200
225
250
275
300
T_red (°C)

Fig. 8

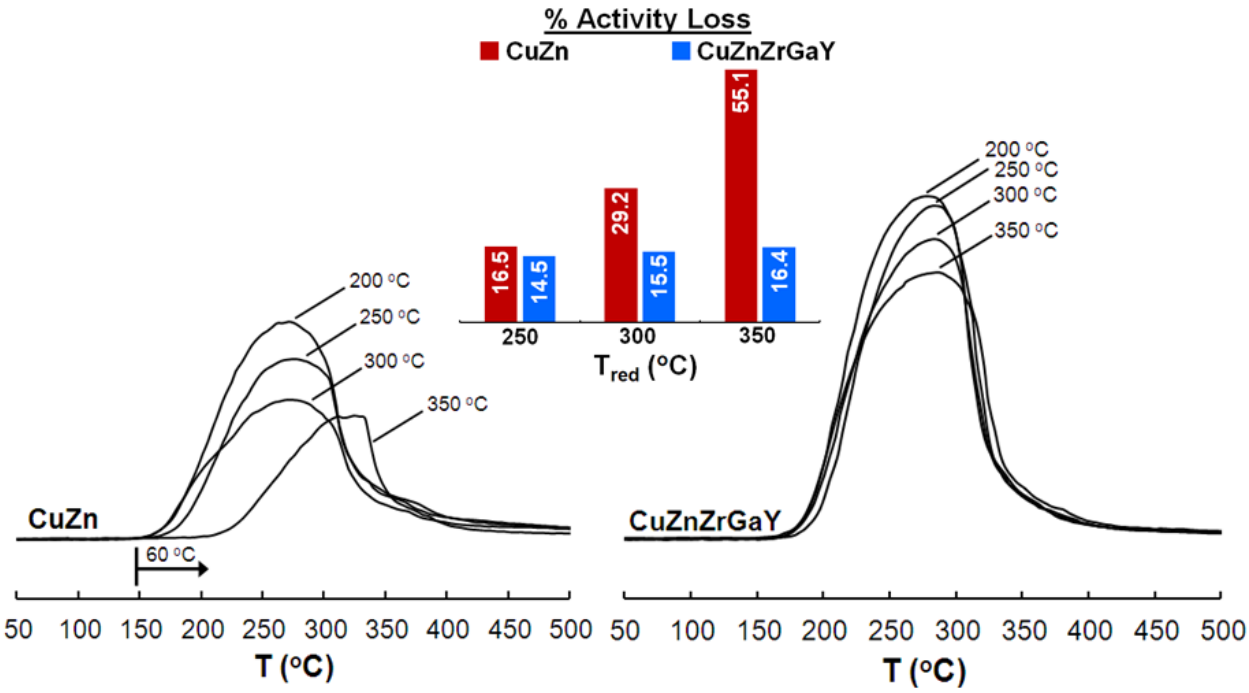
% Activity Loss
CuZn
CuZnZrGaY
16.5
14.5
29.2
15.5
55.1
16.4
250
300
350
T red (°C)
200 °C
250 °C
300 °C
350 °C
60 °C
CuZn
CuZnZrGaY
50 100 150 200 250 300 350 400 450 500
T (°C)